



# Lithospheric expression of cenozoic subduction, mesozoic rifting and the Precambrian Shield in Venezuela



Jeniffer Masy<sup>a</sup>, Fenglin Niu<sup>b,a,\*</sup>, Alan Levander<sup>a</sup>, Michael Schmitz<sup>c</sup>

<sup>a</sup> Department of Earth Science, Rice University, Houston, TX 77005, USA

<sup>b</sup> State Key Laboratory of Petroleum Resource and Prospecting, and Unconventional Natural Gas Institute, China University of Petroleum, Beijing, China

<sup>c</sup> FUNVISIS, Caracas, Venezuela

## ARTICLE INFO

### Article history:

Received 1 May 2014

Received in revised form 28 August 2014

Accepted 31 August 2014

Available online xxx

Editor: P. Shearer

### Keywords:

receiver functions

Caribbean

lithosphere asthenosphere boundary

surface wave tomography

subduction

slab tear

## ABSTRACT

We have combined surface wave tomography with Ps and Sp receiver-function images based on common-conversion-point (CCP) stacking to study the upper mantle velocity structure, particularly the lithosphere–asthenosphere boundary (LAB), beneath eastern and central Venezuela. Rayleigh phase velocities in the frequency range of 0.01–0.05 Hz (20–100 s in period) were measured using the two-plane-wave method and finite-frequency kernels, and then inverted on a  $0.5^\circ \times 0.5^\circ$  grid. The phase velocity dispersion data at grid points were inverted for 1D shear velocity profiles using initial crust–mantle velocity models constructed from previous studies. The 3D velocity model and receiver-function images were interpreted jointly to determine the depth of the LAB and other upper mantle features. The tomographic images revealed two high velocity anomalies extending to more than  $\sim 200$  km depth. One corresponds to the top of the subducting Atlantic plate beneath the Serrania del Interior. The other anomaly is a highly localized feature beneath the Maturin Basin. The LAB depth varies significantly in the study region: it is located at  $\sim 110$  km depth beneath the Guayana Shield, and reaches  $\sim 130$  km at the northern edge of the Maturin Basin, which might be related to the downward flexural bending due to thrust loading of the Caribbean plate and pull from the subducting Atlantic plate. Immediately to the west, the lithosphere is thin ( $\sim 50$ – $60$  km) along the NE–SW trending Espino Graben from the Cariaco basin to the Orinoco River at the northern edge of the craton. The LAB in this region is the top of a pronounced low velocity zone. Westward, the lithosphere deepens to  $\sim 80$  km depth beneath the Barinas Apure Basin, and to  $\sim 90$  km beneath the Neogene Merida Andes and Maracaibo block. Both upper mantle velocity structure and lithosphere thickness correlate well with surface geology and are consistent with northern South American tectonics.

© 2014 Elsevier B.V. All rights reserved.

## 1. Introduction

The Southern Caribbean plate boundary has been formed by interactions between the South America (SA) and Caribbean (CAR) plates since collision of northwestern Venezuela with the Caribbean  $\sim 55$  Ma (e.g. Kellogg and Bonini, 1982; Meschede and Frisch, 1998; Pindell et al., 2005). GPS measurements indicate that the CAR is currently moving approximately 2 cm/yr relative to SA, parallel to the strike slip fault system in the east, with oblique convergence in the west (Perez et al., 2001; Weber et al., 2001; Bilham and Mencin, 2013). The latter results in subduction and underthrusting of the southern edge of the Caribbean beneath

northwestern South America (Fig. 1). Although in eastern and central Venezuela most of the motion is taken up along an  $\sim 80$  km wide shear zone centered on the SS-EP fault zones (Perez et al., 2001), deformation occurs in a broader zone,  $\sim 300$  km wide in eastern Venezuela and up to  $\sim 600$  km wide in western Venezuela and eastern Colombia (e.g. Meschede and Frisch, 1998; Audemard and Audemard, 2002; De Toni and Kellogg, 1993). The plate boundary in western Venezuela is complicated by the motion of the triangular Maracaibo block (MB), a deforming lithospheric block that is escaping northward relative to SA along the Bocono and Santa Marta strike-slip fault systems (Fig. 1). The ranges bounding the MB are the Merida Andes on the east, and the Perija Range and the Santa Marta Massif on the west (Kellogg and Bonini, 1982; Audemard and Audemard, 2002), forming the Eastern Cordillera of the northernmost Andes.

\* Corresponding author.

E-mail address: niu@rice.edu (F. Niu).

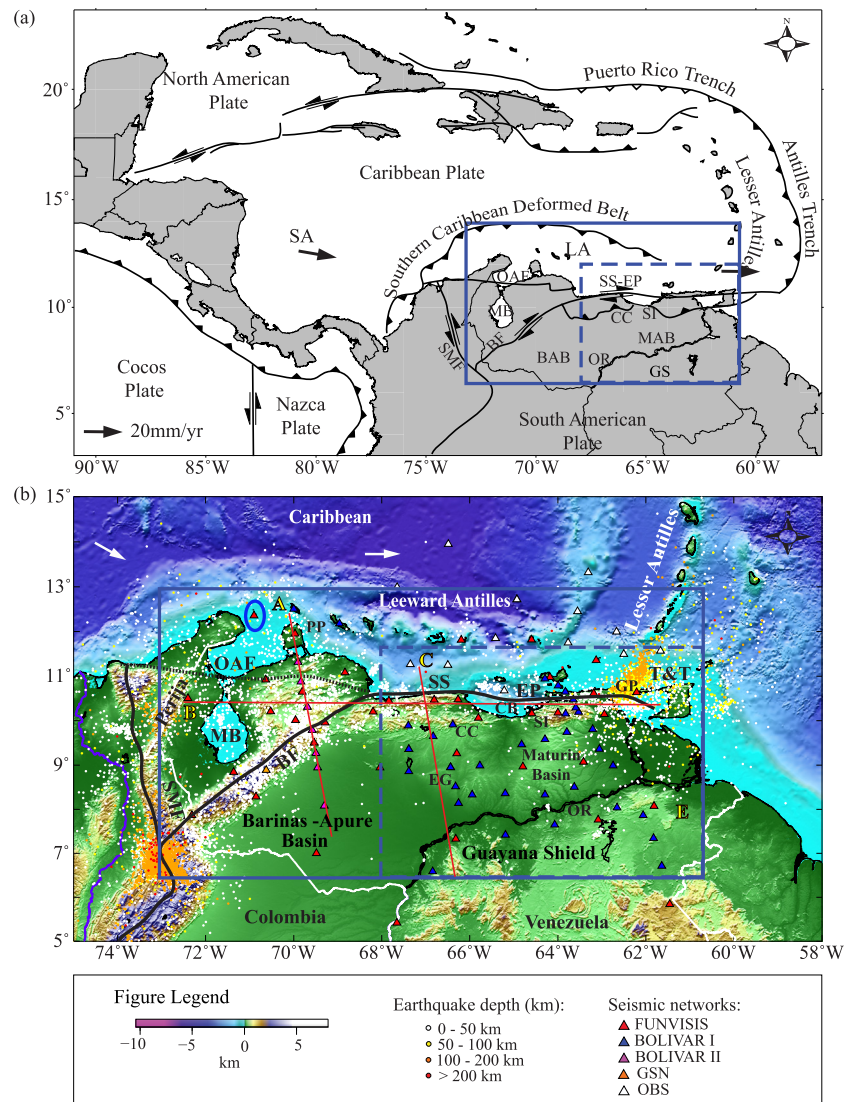


**Fig. 1.** (a) Caribbean tectonics, with GPS vectors in the southern Lesser Antilles Arc and on San Andres (SA) Island in the western Caribbean (Perez et al., 2001). Red box indicates the study area. Blue dashed box indicates study region for the Rayleigh wave tomography. (b) Broadband seismic stations in Venezuela used in the investigation of the LAB. Triangle color indicates different network affiliations. Seismicity at different depths is shown with color-coded circles. Station in blue circle is the station located at Los Monjes Island (IMOV). Locations of 3 profiles (A–C) shown in Figs. 6–8 are indicated. Major faults are indicated as solid black lines. MB: Maracaibo Block, BF: Bocono Fault, OAF: Oca-Ancon Fault (dashed black line); SMF: Santa Marta-Bucaramanga Fault; SS-EP: San Sebastian-El Pilar Fault; BAB: Barinas-Apure Basin; CC: Cordillera de la Costa; SI: Serrania del Interior; OR: Orinoco River; LA: Leeward Antilles. GS: Guayana Shield. GP: Gulf of Paria; EG: Espino Graben; PP: Paraguana Peninsula; MAB: Maturin Basin. (For interpretation of the references to color in this figure legend, the reader is referred to the web version of this article.)

In central and eastern Venezuela, plate motion is accommodated by transpression and transtension along the right lateral San Sebastian–El Pilar strike-slip fault system (Perez et al., 2001; Audemard et al., 2005), a strike-slip system of similar scale to the San Andreas Fault in California. The San Sebastian–El Pilar system marks the northern edge of coastal thrust belts (such as Cordillera de la Costa and Serrania del Interior) and their associated foreland basins (e.g. Guarico and Maturin Basin, Fig. 1). Seismicity along the strike slip boundary is mostly shallow (<50 km; Palma and Romero, 2011), and concentrated along the major strike slip fault systems with more diffuse seismicity on the thrust faults in the Serrania del Interior, the Cordillera de la Costa, and the Mérida Andes (Fig. 1). At its eastern end, the transform motion ends at the southern corner of the Antilles subduction zone, where the Atlantic plates (oceanic lithosphere of the North and South America plates) are subducting beneath the Greater and Lesser Antilles (Molnar and Sykes, 1969; Russo et al., 1993). Intermediate depth seismicity, which ceases abruptly beneath the Gulf of Paria (e.g., VanDecar et

al., 2003; Meighan et al., 2013), has been used to infer the location of the top of the subducting slab to ~200 km depth. The southernmost intermediate depth seismicity cluster, offshore of the Paria Peninsula, has been interpreted as the expression of lithospheric tearing (e.g. Russo et al., 1993; Clark et al., 2008a, 2008b; Meighan et al., 2013), with the transition from subduction zone to strike slip system characterized as a Subduction-Transform Edge Propagator (STEP) boundary (Govers and Wortel, 2005; van Benthem et al., 2013). Tomographic images show a steeply subducting slab and also an aseismic landward continuation of descending lithosphere beneath the Serrania del Interior (VanDecar et al., 2003; Bezada et al., 2010a). These results were interpreted as either convective removal of lithospheric mantle from the continental SA near the subducting Atlantic slab (Bezada et al., 2010a), or northward subduction of the SA passive margin lithosphere (VanDecar et al., 2003). Outcropping of intrusive (~5 Ma) rocks onshore Venezuela (Santamaria and Schubert, 1974; McMahon, 2001), and the location of geothermal systems in eastern Venezuela associated with

a shallow intrusive body (Urbani, 1989) are interpreted as geologic indicators of the presence of the edge of the slab beneath continental SA.

In western Venezuela and eastern Colombia, intermediate depth seismicity and tomographic images suggest that the CAR plate subducts beneath SA offshore of the Santa Marta Massif with a very low angle (Van der Hilst and Mann, 1994; Malave and Suarez, 1995; Taboada et al., 2000). It then dips steeply to ESE under Lake Maracaibo and the Mérida Andes (Pennington, 1981; Taboada et al., 2000; Bezada et al., 2010a), reaching transition zone depths. The flat subduction beneath northern Colombia and westernmost Venezuela is thought to be responsible for the uplift and deformation of the Santa Marta Massif, the Perija range and the Merida Andes (Kellogg and Bonini, 1982; Bezada et al., 2010a). Another viewpoint holds that these ranges are the result of the late Miocene–Pliocene collision of the Panama arc with SA (Molnar and Sykes, 1969).

The Archean–Proterozoic Guayana Shield, part of the Amazonian Craton, underlies southeastern and south-central Venezuela (Gonzalez de Juana et al., 1980). The Archean–Proterozoic Guayana Shield is divided into provinces (Yoris and Ostos, 1997): The Archean Imataca province (3700–3400 My) is in the northern shield just south of the Orinoco River. It is bounded by two Proterozoic provinces: Pastora (2300–1900 My) and Cuchivero (1900–1400 My), to the southeast and southwest, respectively. A fourth Proterozoic province, Roraima (1800–1600 My), lies further south beyond the study area.

In the Cenozoic, northern Venezuela and the continental interior have been affected by a range of geodynamic processes: Subduction, transpression, and transtension have formed the modern plate boundary. The crustal structure of much of Venezuela has been determined from a variety of seismic probes (Schmitz et al., 2002, 2005; Niu et al., 2007; Guedez, 2007; Clark et al., 2008c; Bezada et al., 2008, 2010b; Magnani et al., 2009), and the deeper structure through the transition zone has been determined from regional and global teleseismic tomography (Bezada et al., 2010a; Bijwaard et al., 1998; VanDecar, 2003; Van Benthem et al., 2013). This study is designed to image the structure of the lithosphere and the lithosphere–asthenosphere boundary (LAB) using Rayleigh wave tomography, Ps and Sp receiver functions. This study is part of the BOLIVAR (Broadband Onshore–Offshore Lithospheric Investigation of Venezuela and the Antilles Arc Region) and GEODINOS (Geodinamica Reciente del Limite Norte de la Placa Sudamericana) projects, a joint U.S.–Venezuelan investigation of the structure and evolution of the CAR-SA plate boundary (Levander et al., 2006). The data used here consist of teleseismic events recorded by a 93 station broadband seismic array including land and ocean-bottom seismometers that extended from the Caribbean basin to the Guayana shield (Fig. 1).

## 2. Data and methods

### 2.1. BOLIVAR data set

The data used in this study were recorded by 37 instruments of the Venezuelan National Seismograph Network, 1 GSN station, and two temporary BOLIVAR arrays. The first BOLIVAR deployment included an ~18-month deployment of 27 PASSCAL stations and 8 Rice broadband stations, and a yearlong deployment of 13 OBSIP ocean bottom seismographs in central and eastern Venezuela. The second phase consisted of a 13-month deployment of 7 Rice broadband stations in western Venezuela (Fig. 1b). The 93 stations cover an area of ~1200 km by ~600 km. In eastern Venezuela, station spacing varies from ~10 km to ~100 km, with an average of ~50 km. The FUNVISIS network and the second BOLIVAR

array provide much sparser station spacing in western Venezuela ( $\geq 68^\circ\text{W}$ ).

### 2.2. 3D initial velocity model

Initial crustal velocity models including constraints on Moho depths are important for inverting for shear velocity from surface wave dispersion data and in estimating depth of mantle discontinuities using receiver function data. We first constructed a 3D P-wave velocity model of the crust through interpolation of 2D P-reflection and reflection/wide-angle seismic data (Schmitz et al., 2002, 2005; Guedez, 2007; Clark et al., 2008c; Bezada et al., 2010b; Magnani et al., 2009). We used the empirical relationship between P- and S-wave velocities of crustal rocks compiled by Brocher (2005) to estimate crustal shear wave velocity structure. Crustal thickness was compiled from the active-source seismic data cited above and passive receiver function data (Niu et al., 2007). We also included 3D mantle velocity structure obtained from finite-frequency P-wave tomography (Bezada et al., 2010a) in our initial model. S-wave velocity in the mantle was computed using the  $V_p/V_s$  ratio of the AK135 model (Kennett et al., 1995).

### 2.3. Receiver functions analysis

Receiver functions have been widely used to estimate Moho depth and to image seismic discontinuities in the mantle. In a layered medium, a teleseismic record can be considered as the summation of the direct arrival and a series of conversions and reflections at boundaries below the station. Receiver functions are an attempt to approximate a Green's function associated with structure beneath the receiver by deconvolving one component of a teleseismic signal from another to remove source signals from seismograms (Ammon, 1991). For instance, deconvolving the vertical (or longitudinal) component from the radial (or in plane shear) component helps to isolate the P-to-S converted waves, generating a Ps receiver function. We selected a total of 833 Ps receiver functions generated from 48 events with  $M_w \geq 6$  and epicentral distances between  $35^\circ$  and  $90^\circ$  recorded by the BOLIVAR array (Fig. 2a).

The procedure to generate Sp receiver functions is similar to the method of calculating Ps receiver functions. In this case, the in-plane S wave and its precursors are deconvolved from the longitudinal component to isolate S-to-P converted arrivals before the direct S (Yuan et al., 2006). In the Ps receiver function data, P-to-S conversions from upper mantle structures, such as the LAB may interfere with crustal multiples, making it difficult to image the LAB with Ps receiver function data. Since S-to-P conversions arrive prior to direct S, and multiple reflections arrive after S, such interference does not exist in the Sp receiver function data. The lower frequencies are also more appropriate for imaging gradual velocity transitions such as a thermally controlled LAB. On the other hand, the spatial resolution of Sp receiver function data is about 5 times coarser than that of the Ps receiver functions (Levander et al., 2011) due to the lower frequency content of S-wave signals (Yuan et al., 2006). We chose 42 events with  $M_w > 5.7$  and epicentral distances between  $55^\circ$  to  $85^\circ$  during the period of 2003–2009 to generate a total of 656 Sp receiver functions (Fig. 2a).

The Ps receiver functions we present in this study have a shaping filter with high corner frequencies of 0.5 Hz and 1 Hz, while the Sp receiver functions have 0.2 and 0.1 Hz shaping filters. Receiver functions were calculated using both iterative deconvolution (Ligorria and Ammon, 1999) and water level deconvolution (Ammon, 1991). We found that there are no significant differences between the two sets of the receiver functions.

Given a velocity model, one can use the time differences between converted waves and the direct arrival to estimate the

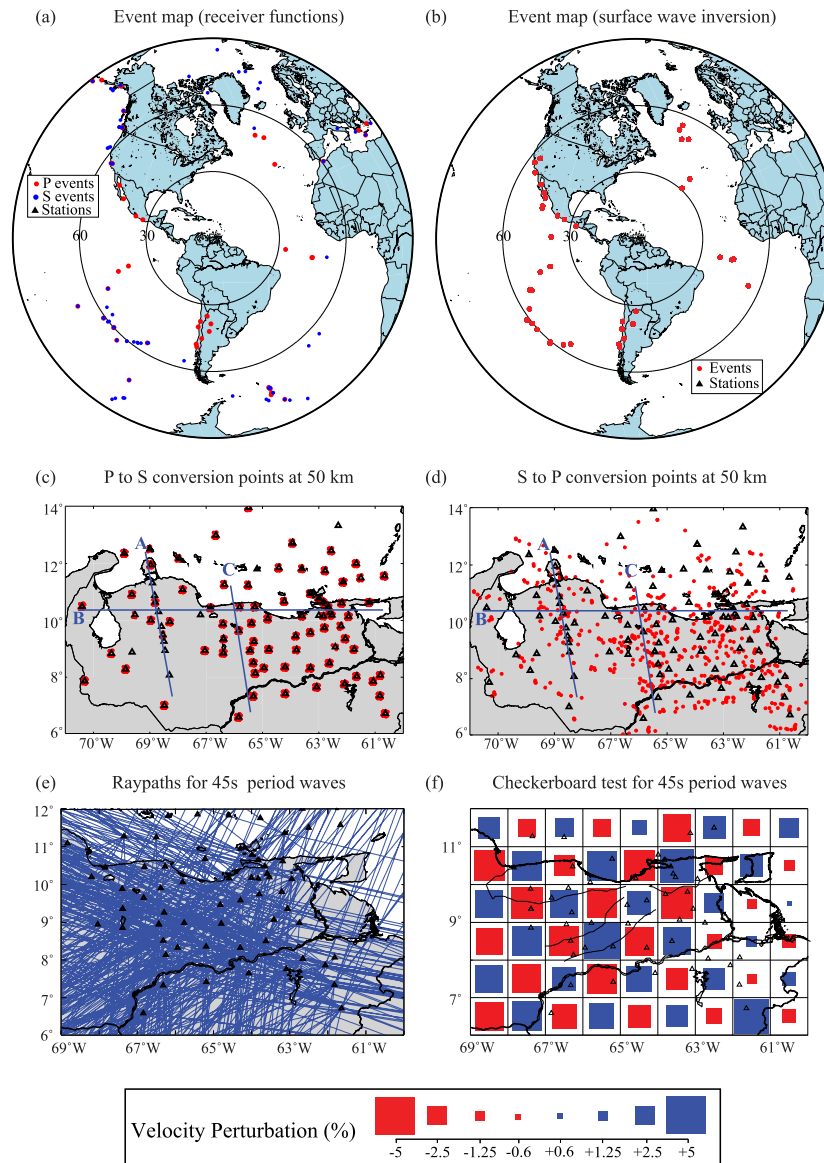


**Fig. 2.** (a) Location of the 48 events between 35° and 90° used for the Ps receiver function (red dots) and of the 42 events between 55° and 85° used for the Sp receiver function (blue dots). (b) Location of 45 events at distances >30° used for the Rayleigh wave tomography (red dots). (c)–(d) Distribution of the conversion points of the Ps and Sp phases at 50 km depth. (e) Raypath coverage for Rayleigh waves with a period of 45 s. (f) Checkerboard test for Rayleigh waves with a period of 45 s. Triangles indicate the broadband stations in the study area. Profile location is indicated in (c) and (d). (For interpretation of the references to color in this figure legend, the reader is referred to the web version of this article.)

**Table 1**  
Phase velocity inversion data.

Frequ. (mHz)	Period (s)	Average phase velocity (km/s)	Phase velocity error	Number of raypaths	Number of events	Wavelength (km)
50	20	3.502	0.0431	442	38	70
45	22	3.580	0.0369	625	39	78
40	25	3.671	0.0525	621	37	92
37	27	3.725	0.0453	617	41	100
33	30	3.812	0.0533	653	45	114
29	34	3.888	0.0314	369	21	132
25	40	3.938	0.0413	374	21	158
22	45	3.980	0.0539	617	39	180
20	50	3.999	0.0531	566	39	201
17	59	4.022	0.0315	429	36	237
15	67	4.044	0.0414	481	39	270
13	77	4.049	0.0314	412	34	312
11	91	4.054	0.0514	367	30	370
10	100	4.118	0.0315	337	31	412

depths of the Moho and deeper boundaries in the mantle, such as the LAB. To improve the signal-to-noise ratio (SNR) of the P-to-S converted arrivals, we applied the common-conversion-point (CCP) stacking method (Dueker and Sheehan, 1997) with the implementation described in Levander and Miller (2012). More specifically, we divided the study area ( $6.5^{\circ}\text{N}$  to  $13^{\circ}\text{N}$ ,  $72^{\circ}\text{W}$  to  $61^{\circ}\text{W}$ ) into a  $0.25^{\circ}$  by  $0.25^{\circ}$  grid and used a circular cap with a radius of  $0.75^{\circ}$  and  $1^{\circ}$  to gather and stack the Ps and Sp receiver functions, respectively. We also considered approximately elliptical Fresnel zones of the conversion phases in gathering receiver functions in each cap. The transverse diameter of the Fresnel zone at 50 km depth is  $\sim 0.2^{\circ}$  and  $\sim 5.9^{\circ}$  for a Ps and Sp conversion phases with a dominant frequency of 1 and 0.2 Hz, respectively. In Fig. 2c and 2d, we show the distribution of the specular conversion points of the Ps and Sp phases at 50 km depth. The Ps conversion points cluster more closely to the stations than do the Sp conversions since the Ps rays have much steeper incidence angles than Sp rays. Thus the lateral continuity of the Ps receiver function images is relatively poor, especially in the western part of the study area.

#### 2.4. Finite frequency Rayleigh wave tomography

In order to determine the three-dimensional shear wave velocity structure within the study area, we used the two-step inversion technique developed by Yang and Forsyth (2006a). The first stage involves computing 2-D phase velocities using the two plane-wave method (Forsyth and Li, 2005; Yang and Forsyth, 2006a, 2006b). This method accounts for effects due to multipathing of the incoming wavefield. Finite-frequency amplitude and phase sensitivity kernels were used to improve lateral resolution (Yang and Forsyth, 2006b). A previous investigation of this area using the same dataset (Miller et al., 2009) did not make use of the finite-frequency kernels to determine phase velocities. Also one concern on Miller et al. (2009) is that the study area might be too large to be suitable for the existing two-plane wave method. We thus decided to divide the study area of Miller et al. (2009) into two, and conducted surface wave inversion separately. We found that the western area (west to  $68^{\circ}\text{W}$ ) is not suitable for the inversion because of the very limited data coverage and the limited bandwidth of the sensors ( $\sim 40$  s–50 Hz).

Considering the above factors, we re-parameterized the original study area ( $12^{\circ} \times 8^{\circ}$ ) used by Miller et al. (2009), into a smaller area of ( $7^{\circ} \times 5^{\circ}$ ) in eastern Venezuela, between  $61^{\circ}\text{W}$  to  $68^{\circ}\text{W}$  longitude and  $6.5^{\circ}$  to  $11.5^{\circ}$  latitude (Fig. 1), with a grid spacing of  $0.5^{\circ} \times 0.5^{\circ}$ . Two additional layers of grids with the same grid spacing are used to surround the study area in order to absorb errors not accounted for by the two-plane wave approximation. Within this area there are 53 stations from the combined FUNVISIS/BOLIVAR array (Fig. 1). We analyzed data from a total of 45 earthquakes within a distance range of  $30^{\circ}$  to  $120^{\circ}$ , and magnitude greater than 5.7 that occurred between December 2003 and May 2005 (Fig. 2b). As shown in Fig. 2c, we have moderately dense raypath coverage (Fig. 2e, Table 1).

We first performed a standard checkerboard test with two synthetic velocity models consisting of  $0.5^{\circ} \times 0.5^{\circ}$  and  $1^{\circ} \times 1^{\circ}$  cells, respectively. The cells have alternating positive and negative 5% velocity perturbations from a uniform background model with  $V_s = 3.558$  km/s. Synthetic phase velocity data were computed along the 625 raypaths measured at 45 s period (Fig. 2e). We inverted the synthetic data utilizing the same parameterization employed in the inversion of real data. We found that our data coverage is not dense enough to evenly recover the  $0.5^{\circ} \times 0.5^{\circ}$  checkerboard anomalies, but are able to resolve the  $1^{\circ} \times 1^{\circ}$  patterns very well (Fig. 2f). We also conducted similar tests with the raypath coverage of other periods to ensure that each period has enough data to

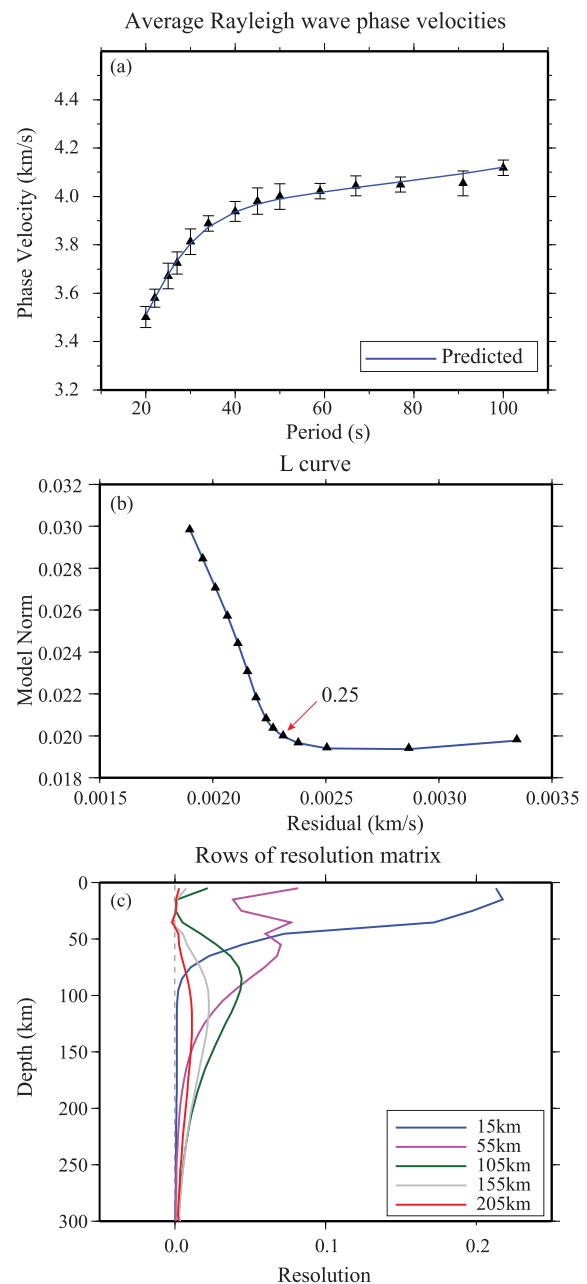


**Fig. 3.** (a) Average Rayleigh wave phase velocities at 14 periods ranging from 20 to 100 s. Error bars represent two standard deviations. (b) Model norm is shown as a function of the phase velocity residual norm (km/s) for various damping parameters. The optimum value of the damping parameter is the elbow of the L-shaped curve. (c) Model resolution kernels for layers at depths of 15, 55, 105, 155, and 205 km. (For interpretation of the references to color in this figure legend, the reader is referred to the web version of this article.)

resolve the  $1^{\circ} \times 1^{\circ}$  cells. The lateral resolution of our data is thus expected to be  $\sim 100$  km in most places, and could reach  $\sim 50$  km in some densely instrumented areas.

We inverted for the isotropic phase velocities at all the periods ranging from 20 to 100 s on a  $0.5^{\circ} \times 0.5^{\circ}$  grid (Table 1). Fig. 3a shows the observed average phase velocities of the study area, which vary from 3.488 km/s at 20 s to 4.122 km/s at 100 s (Table 1). Fig. 4 shows phase velocity variations for six different periods; each period shows significant lateral variations. At 20 s and 25 s periods, corresponding to crustal structures (Fig. 4a and 4b), we observe a very slow anomaly ( $\sim -6$  to  $-4\%$ ) beneath the Serrania del Interior that extends east towards Trinidad, and west

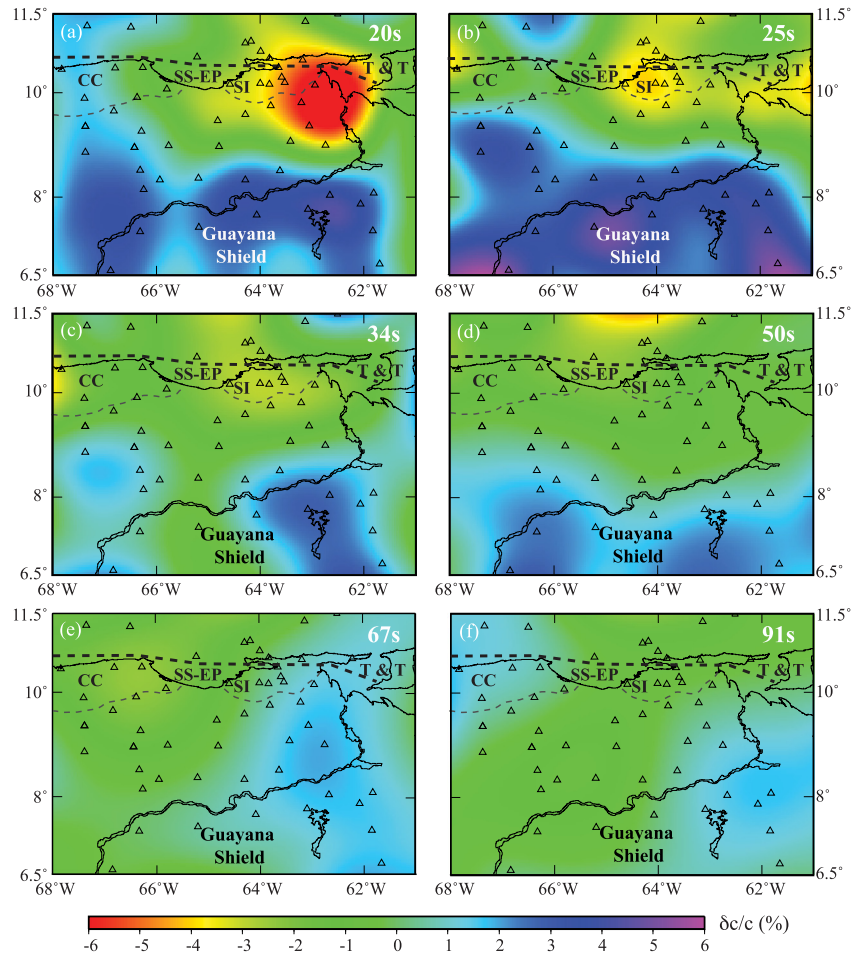


**Fig. 4.** Phase-velocity perturbations at periods of 20, 25, 34, 50, 67, and 91 s. Phase velocity inversions were conducted with a grid spacing of  $0.5^\circ \times 0.5^\circ$ . The thick and thin dashed lines indicate the San Sebastian–El Pilar Fault, and the thrust front of the coastal cordillera. Abbreviations are same as Fig. 1. Note that the western part of the Guayana shield is featured by low velocity at the 34 s phase-velocity map, but exhibits relatively high velocity on the 25 s and 50 s map, which might be caused by lateral variations in Moho depth. (For interpretation of the references to color in this figure legend, the reader is referred to the web version of this article.)

to the Cariaco basin. At almost all periods, the Guayana Shield shows a persistent higher-than-average velocity compared to the surrounding regions (Figs. 4a to 4f). At 34 s there is a high velocity anomaly at  $\sim 63^\circ\text{W}$  beneath the Guayana Shield (Fig. 4c).

We inverted the phase velocity dispersion for 1D Vs structure at each grid point using DISPER80 code (Saito, 1988), employing as initial models the 3D starting velocity model described in Section 2.2. We tested various damping parameters, calculated the L curve, and selected an optimum value of 0.25 (Fig. 3b). The optimum value of the damping parameter agrees with those used in previous studies that employed the same inversion method (Schutt et al., 2008; Liu et al., 2011). We finally assembled the resulting 1D shear velocity profiles at each grid point forming a pseudo-3D velocity volume that extends to a depth of  $\sim 200$  km (Fig. 5). The 3D Vs model is described below.

### 3. Results and discussion

In the following sections, we will describe the main features from the receiver function and surface wave tomography images from the crust down, followed by a discussion of geodynamic implications.

#### 3.1. Crustal structure

Since crustal studies have been conducted previously using BOLIVAR wide-angle seismic (Schmitz et al., 2002; Guedez, 2007;

Clark et al., 2008c; Magnani et al., 2009; Bezada et al., 2010b) and receiver function data (Niu et al., 2007), the primary focus here is not Moho depth, although our observations of Moho depth are consistent with the previous results.

Fig. 6 shows the CCP stacked images along a relatively densely instrumented line (Profile A in Fig. 1) in western Venezuela. The Ps receiver function (Fig. 6a) reveals a sub-moho structure at 40 km to 60 km, dipping at an angle of  $\sim 15^\circ$  towards the continent beneath the Paraguana Peninsula. This feature is much weaker in the Sp receiver function image (Fig. 6b). At low frequency, the Sp conversions at the Moho and the sub-moho structure might interfere with each other. We thus attribute the observation to either this interference, or the low Sp data coverage in the area, or both (Fig. 2d). The sub-moho structure was also seen on the stacked receiver function of the station IMOV located at the Los Monjes island (Fig. 1) in the study of Niu et al. (2007). Bezada et al. (2008) observed a clear arrival in a long offset active-source seismic profile roughly collocated with the Profile A, and interpreted it as reflections from the Moho of the CAR under northwestern Venezuela. Our image here is consistent with these studies, and we interpret the dipping structure here is the Moho of the underthrust CAR.

A sub-moho feature is also clearly seen in the EW depth section of Ps CCP image at  $\sim 60$  km depth below the northwestern edge of the Maracaibo block (Fig. 7, Profile B in Fig. 1). No event is seen in the corresponding Sp image, which we attribute to low fold (Fig. 2d). The event dips east with an angle of  $\sim 17^\circ$ .

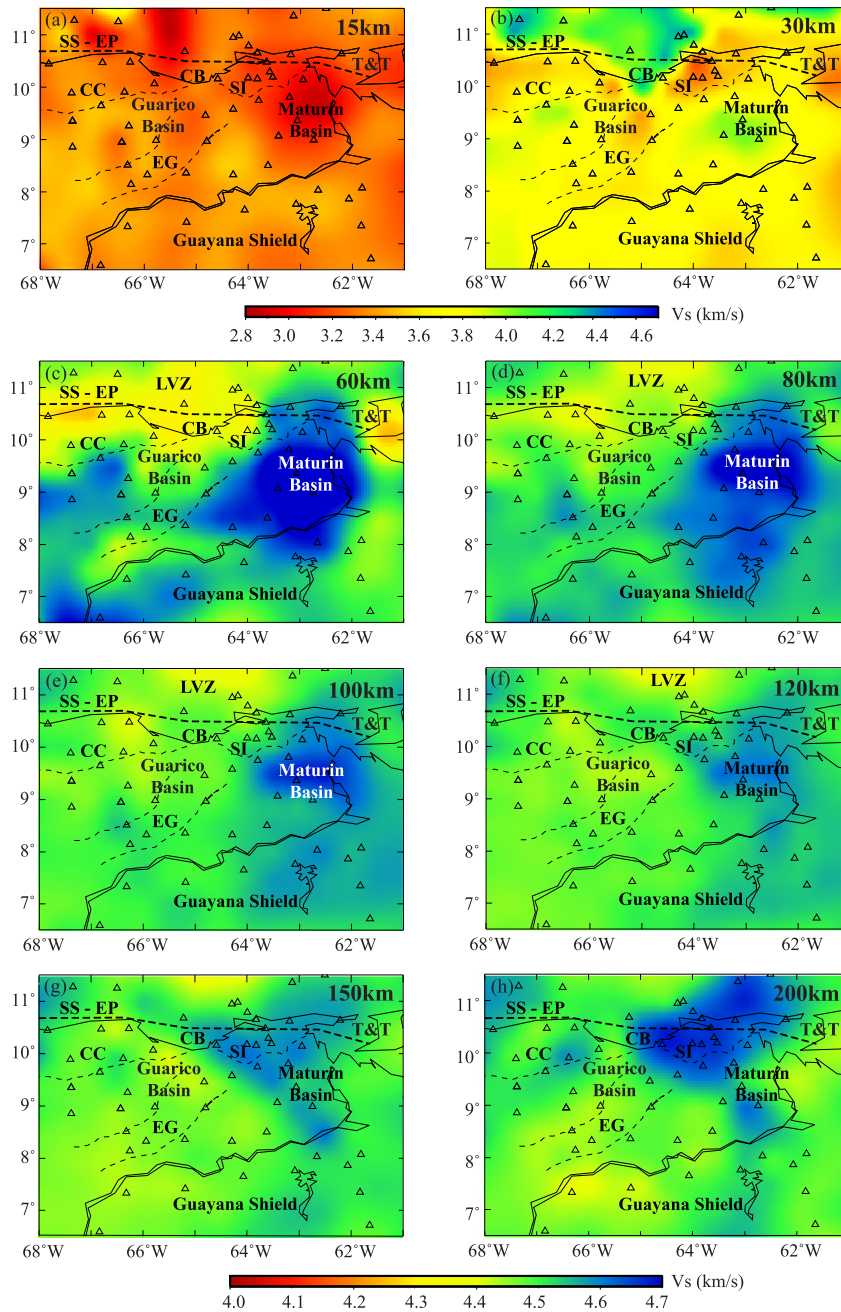


**Fig. 5.** Lateral variations of shear wave velocity at different depths as indicated on the figure. SS-EP: San Sebastian–El Pilar Fault system; CC: Cordillera de la Costa; SI: Serrania del Interior; EG: Espino Graben; CB: Cariaco Basin. Note a low velocity zone (LVZ) extending to  $\sim 100$  km beneath the Cariaco Basin, and two deep ( $>150$  km) high-velocity anomalies beneath the SI and the southern Maturín Basin. (For interpretation of the references to color in this figure legend, the reader is referred to the web version of this article.)

The observed dip angle here is lower than the true dip because CCP stacking does not restore dips to the proper angle. It agrees reasonably well with values derived from the Wadati-Benioff seismicity beneath northern Colombia, i.e.,  $20^\circ$  by Pennington (1981) and  $25^\circ$  by Malave and Suarez (1995). The dipping structure disappears beneath Lake Maracaibo at  $\sim 70$  km depth just west of the Merida Andes (Fig. 7), where finite-frequency P wave tomography (Bezada et al., 2010a) shows that the Caribbean slab starts to subduct steeply. Thus this dipping converter is also likely the Moho of the CAR plate subducting from west to east beneath SA.

Bezada et al. (2010a) and Masy et al. (2011) proposed that the Caribbean plate is torn between the northern and southern Maracaibo Block in the vicinity of the Oca–Ancon Fault zone. We show a cartoon of the hypothesized tear in Figure S1. Profiles A

and B (Figs. 6 and 7) are consistent with slab tearing, as the slab is present at shallow depth north of the Oca, but to the south is imaged only west of Lake Maracaibo. North of the Oca Fault the CAR plate underthrusts the SA continental margin, south of the Oca Fault the plate is subducting steeply beneath the Lake Maracaibo and the Merida Andes, as seen in teleseismic tomography (Bezada et al., 2010a). The areas north and south of the putative slab tear also show distinctly different deformation styles. The northeastern region is characterized by a broad uplift (i.e., the Serrania de Falcon) with widespread faulting and diffuse seismicity. The southwestern region, on the other hand, is featured by narrow Laramide-style basement faulted uplifts, such as, the Merida Andes and the Perija range, and concentrated seismicity.

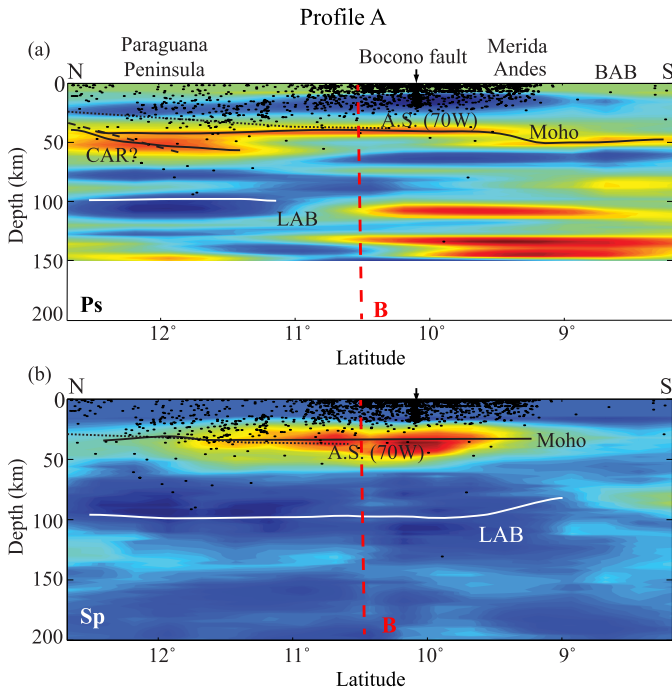


**Fig. 6.** CCP stacked images of the Ps (a) and Sp (b) receiver functions along profile A (see Fig. 1). Red and blue indicate positive (low to high) and negative (high to low) velocity jumps, respectively. The polarity of the Sp receiver functions has been reversed to conform to Ps. Black and white solid lines indicate our interpretation of the Moho and LAB. The dotted line represents the Moho from active source (AS) data along the 70° west line (Guedez, 2007; Bezada et al., 2008). The second black line labeled with “CAR?” at the left side of the Ps image in (b) is interpreted as the subducted Caribbean plate beneath SA interpreted by Bezada et al. (2008). Seismicity within 50 km of the profile is indicated by small black dots. A white mask is over the portion of the Ps CCP image that is contaminated with crustal multiples. The red dashed line shows the intersection with Profile B. (For interpretation of the references to color in this figure legend, the reader is referred to the web version of this article.)

In central Venezuela beneath the Cordillera de la Costa, we find a Ps conversion above the Moho at ~35 km depth that extends from the Bocono fault to the Serrania del Interior (Figs. 7 and 8). Lower frequency Sp receiver functions are incapable of resolving such a feature. The CAR-SA plate boundary in central Venezuela has been transpressional, accommodated by dextral shear on the San Sebastian–El Pilar Fault system accompanied by shortening within the Cordillera de la Costa thrust belt, where SA passive margin, and CAR arc and HP/LT terranes were thrust onto the South American margin (e.g., Jacome et al., 2003). We interpret the 35 km depth Ps conversion as resulting from a detachment surface between the allochthonous terranes thrust onto the northern edge of the South America continent. The upper and lower sides of the surface comprises of relatively low velocity sedimentary rocks and high velocity continental lower crustal rocks, respectively, creating a sharp and strong velocity boundary along the surface. Although somewhat deeper, the intracrustal Ps conversion and the Moho are reasonably consistent with the active source wide-angle imaging along this profile described in Magnani et al. (2009). An intracrustal reflector was identified as the top of a reflective lower crustal layer. Here we interpret this feature as the top of the deepest detachment bounding allochthonous terranes.

### 3.2. LAB and upper mantle structures

The lithosphere is usually referred to as the mechanically strong layer that acts as a rigid plate (e.g. Fischer et al., 2010; Lee et al., 2011); the LAB thus, is a rheological boundary separating the rigid lithospheric lid from the mechanically weaker asthenosphere

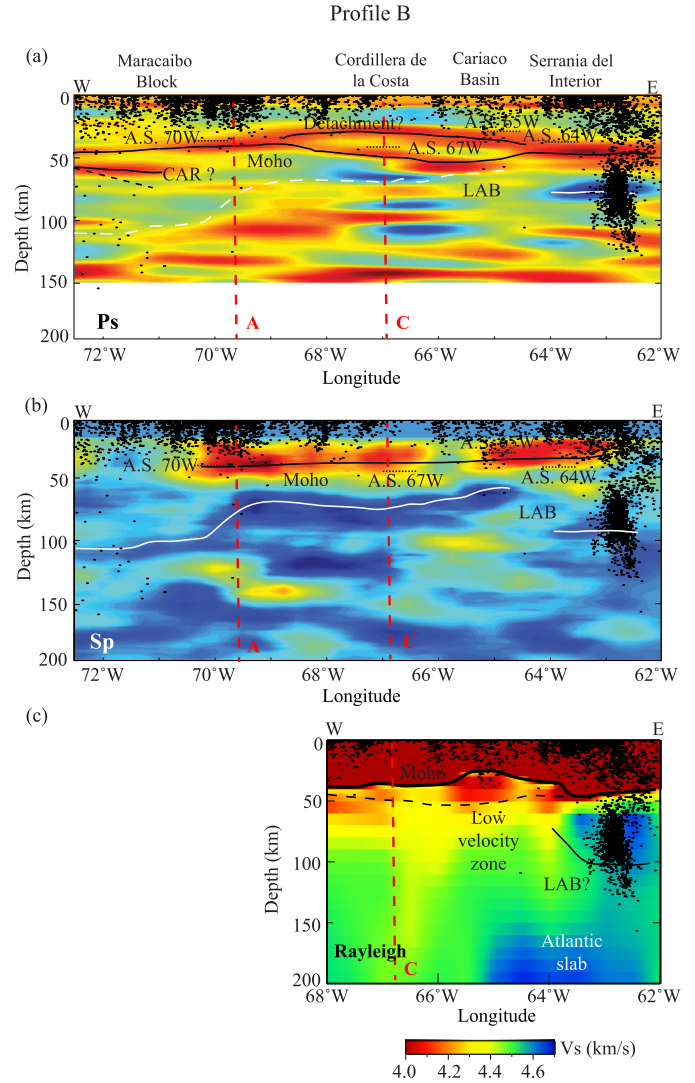


**Fig. 7.** CCP stacked images of the Ps (a) and Sp (b) receiver functions along profile B (see Fig. 1). (c) S-wave velocity inverted from Rayleigh wave dispersion data. The two solid black lines in (c) are the input Moho and the picked LAB, respectively. The long white dashed line in (a) and (b) denotes the LAB location derived from the surface wave data. Active-source (AS) estimates of the Moho at 70°W (Guedez, 2007; Bezada et al., 2008), 67°W (Magnani et al., 2009), 65°W (Bezada et al., 2010b), and 64°W (Clark et al., 2008c) are also shown in (a) and (b). The shallower event beneath the Cordillera de la Costa in (a) is interpreted as the base of overthrust SA passive margin and CAR island arc terranes. The deep tilted event beneath the Maracaibo Block in (a) is the top of the subducting Caribbean plate. Black dashed line represents the top of the subducted Caribbean plate interpreted from body wave tomography by Bezada et al. (2010a). A white mask is over the portion of the Ps CCP image that is contaminated with crustal multiples. The two red dashed lines indicate the intersections with other Profiles A and C. (For interpretation of the references to color in this figure legend, the reader is referred to the web version of this article.)

(Fischer et al., 2010). Vertical gradients of geophysical properties have been used as a proxy to identify the LAB, for example, a negative seismic velocity gradient, a negative seismic impedance gradient, or a rapid change in temperature gradient (Fischer et al., 2010).

We used the Rayleigh wave tomography model and the receiver function data together to make two separate, largely consistent, LAB depth estimates. It can be challenging to identify the LAB from receiver function data when there are either multiple peaks or essentially no distinct peaks in the stacked traces. The latter occurs if the LAB is such a gradual boundary that it generates little S-to-P or P-to-S converted energy (Yuan and Romanowicz, 2010).

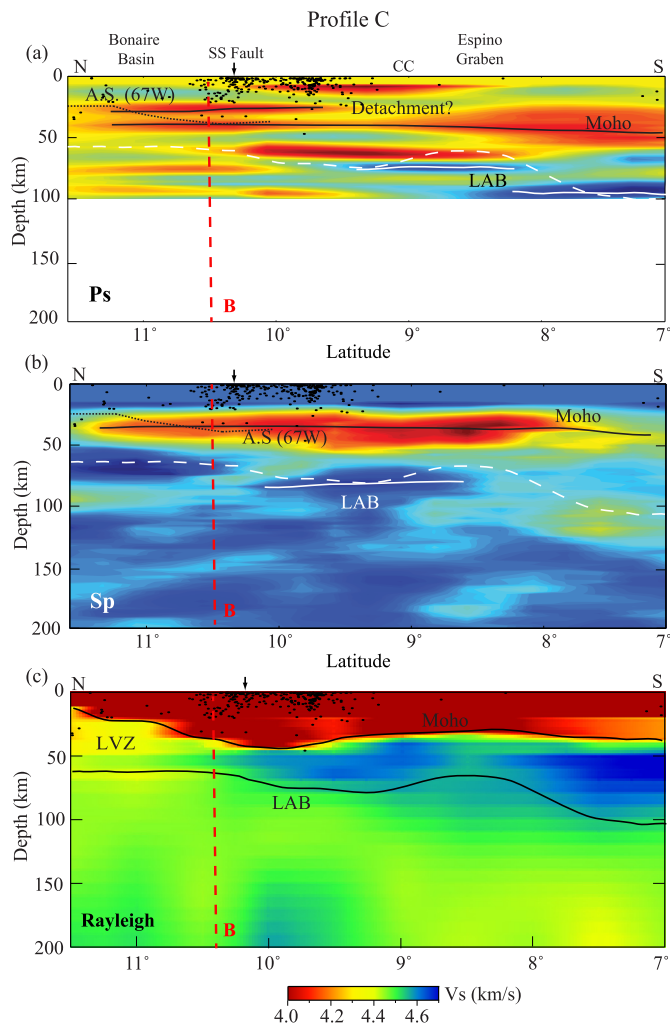


**Fig. 8.** (a)–(c) Ps, Sp and Vs cross-sections along Profile C (see figure). The shallow solid line marked with “Detachment?” in (a) is interpreted as the base of the overthrust Caribbean plate. Moho estimates from active-source (AS) data are the 67° west line analyzed by Magnani et al. (2009). A white mask is over the portion of the Ps CCP image that is contaminated with crustal multiples. The red dashed line shows the intersection with Profile B. There is a strong Ps event at ~10 km in the middle of the Ps receiver function image show in (a), which we interpret as the base of the sediment. The deeper event at ~60 below it could be a sediment-related multiple. (For interpretation of the references to color in this figure legend, the reader is referred to the web version of this article.)

Thus, the additional constraints provided by the surface wave tomography model have been used with the receiver functions. For the CCP stacked Ps and Sp receiver function traces, we identify negative (Ps) or positive (Sp) peaks at depth range between 50 and 200 km as a potential LAB. From the surface wave tomography shear velocity model, following Fischer et al. (2010), we define the LAB as the center of the shallowest negative velocity gradient beneath the Moho in each velocity profile (Fig. 9). As shown in Fig. 9, most of the velocity profiles start with a relatively steep velocity drop, followed by a gradual recovery in velocity as depth increases, thus the center of the shallowest negative velocity gradient usually agrees with the largest negative velocity gradient. Since the LAB may represent a boundary between a dry, cold, deplete lithosphere and a wet, warmer and fertile asthenosphere, the largest velocity drop in the upper mantle may occur at this boundary. In this case the LAB represents the largest negative velocity gradient. We also repeated the surface wave tomography Vs inversions using a 1D initial model, AK135 (Kennett et al., 1995) and found that the negative velocity gradient is a robust structure. We choose a LAB

that is consistent between the datasets; for instance, we select the one that is closest to the value from the surface wave data when several peaks are present in the receiver function data. If there are no distinct peaks in the RF CCP stack, we take the value from the surface wave Vs model. Lateral variations of the LAB depth estimated from receiver function and surface wave data are shown in Figs. 10a and 10b, respectively, with an error of  $\pm 10$  km estimated with a bootstrap method (Efron and Tibshirani, 1986). In general, the LAB depths estimated from the two types of data agree reasonably well ( $< 7\%$  difference on average), while the map resulting from surface wave data appears to have better lateral resolution than the receiver function map. In western Venezuela where there is no overlap between the 2 datasets, we estimated LAB depth from the receiver functions only.

The estimated lithosphere thickness shows a significant variation across the study area, and it seems that lithosphere beneath eastern Venezuela is significantly thicker than the one beneath western and central parts of the Venezuela (Fig. 10). In particular, lithosphere beneath the Serrania del Interior east to the slab tear at  $\sim 64^\circ\text{W}$  is around 110–130 km thick, and is only 55–90 km beneath Cordillera de la Costa. We think this difference is caused by the eastward migration of the Atlantic subduction. The descending Atlantic oceanic lithosphere can viscously remove the lower part of the continental lithosphere from its adjacent orogens.

The observed lithosphere thickness also seems to show some correlation with surface geology and tectonics. The largest change in LAB depth (Fig. 10) is between central and eastern Venezuela roughly along the  $64.5^\circ\text{W}$  meridian, between the Espino Graben in the Guarico Basin and the adjacent Maturin Basin and Serrania del Interior. The lithosphere thickens eastward from  $< 60$  to 80 km depth under the Espino Graben to 100 to 130 km depth under the Maturin Basin and Serrania del Interior (Fig. 10b). The NE–SW oriented Espino Graben was formed during the opening of the Atlantic Ocean in Jurassic (Burke, 1977). It was expected to have a thin lithosphere at the initial stage, but a thermal lithosphere would have re-established itself by the long-term cooling after the rifting episode. The base of thermal lithosphere is less viscous than a dry and compositionally distinct cratonic lithosphere, and thus is relatively easier to be removed by the Atlantic subduction, as explained above.

East to  $\sim 64.5^\circ\text{W}$ , the LAB reaches  $\sim 130$  km deep beneath the Serrania del Interior and the Maturin Basin, which might result from flexure of the SA lithosphere in response to the loads imposed on the SA plate from the thrust belt and the downward pull from the subducting Atlantic slab (Jacome et al., 2003). Southward, the lithosphere thins slightly under the Guayana Shield to 110 to 120 km, roughly consistent with the depth extent of a fast velocity anomaly beneath the same region revealed by the finite-frequency body wave tomography of Bezada et al. (2010a). It also seems that changes in lithosphere thickness within the shield somehow correlate with surface geology (Fig. 10). The Archean Imataca and the Paleo–Proterozoic Pastora provinces have a somewhat deeper LAB ( $\sim 110$ – $120$  km) than the Proterozoic Cuchivero province ( $\sim 80$ – $110$  km). Such a variation might be related to difference in cooling time.

West of the  $64.5^\circ\text{W}$  meridian the LAB is  $\sim 50$  km deep under the offshore Cariaco basin, deepens southwestward to 60–70 km along the axis of the Jurassic Espino Graben (Fig. 10). The thin lithosphere beneath the Cariaco basin could be related to the pull-apart extension occurring in the area, which is believed to be the origin of the basin (Escalona et al., 2011) and also results in a passive upwelling that corresponds to the observed low velocity beneath it. Further to the west, the lithosphere is slightly thicker,  $\sim 60$ – $80$  km thick beneath the Barinas Apure Basin. The lithosphere varies between  $\sim 60$  and 90 km beneath the Neogene Merida Andes, Maracaibo block, and Serrania de Falcon.

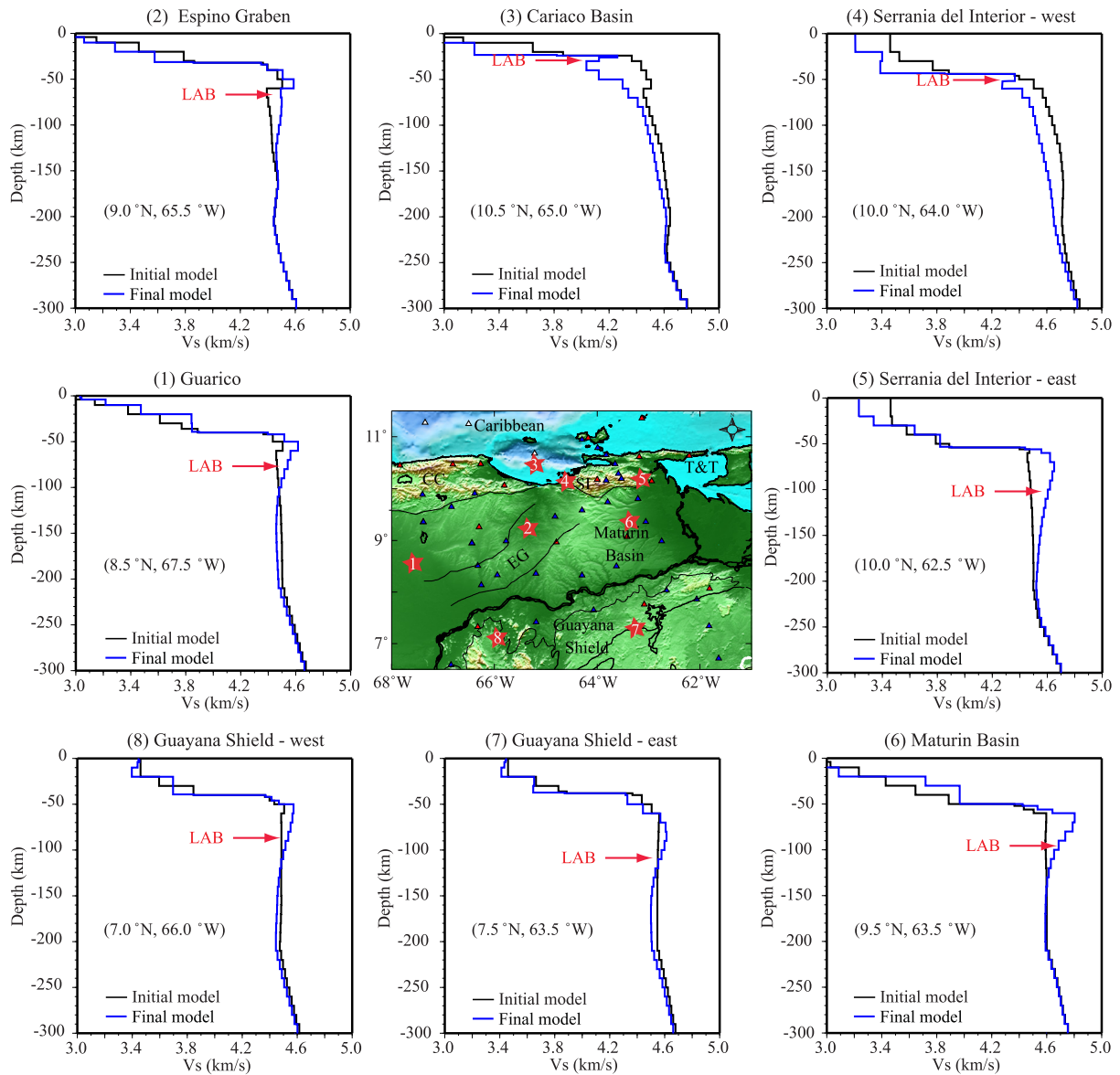


**Fig. 9.** Inverted shear-wave velocity models (blue) and the initial velocity model (black) at 8 locations in the map. (For interpretation of the references to color in this figure legend, the reader is referred to the web version of this article.)

In addition to the LAB structure, the Rayleigh wave tomography also shows several interesting features in the uppermost mantle, the most prominent being the distinct high velocity structure (4.6–4.7 km/s) extending from 60 to at least 200 km depth beneath the southeastern corner of Antilles subduction zone, the Serrania del Interior and the Maturin basin (Fig. 5c to 5h). Consistent with deeper seismicity and previous body wave tomography studies (VanDecar et al., 2003; Bezada et al., 2010a) the northern part of the high velocity anomaly is interpreted as the subducting Atlantic oceanic lithosphere (Fig. S2). We note that at 200 km depth this feature extends across the SA-CAR plate boundary, the El Pilar Fault zone, to the southern edge of the Serrania del Interior (Fig. S3).

The southward extension of the high velocity structure suggests that the geodynamic processes onshore eastern Venezuela are more complicated than a simple transition from transform motion to subduction (e.g. Molnar and Sykes, 1969), defined by a clean tear through the whole lithosphere (Clark et al., 2008a; Govers and Wortel, 2005) at the Paria Peninsula. VanDecar et al. (2003)

suggested that this high velocity anomaly is a detached oceanic lithosphere associated with northward subduction of the SA continental margin. Bezada et al. (2010a) argue that a simultaneous subduction of the margin to the north under the CAR, and of the Atlantic to the west under the CAR is geometrically difficult to achieve. They proposed instead that the high velocity anomaly that extends south of the strike-slip system results from convective removal of the SA continental margin lithospheric mantle driven by the descending Atlantic slab (Fig. 11 in Bezada et al., 2010a). Although it is difficult to distinguish between the two interpretations directly from our tomographic images, the latter provides a better explanation of the observed lithosphere thickness variation under SA as described before, and it is also geometrically difficult to achieve a simultaneous subduction toward the north under the Caribbean and towards the west under the Lesser Antilles.

Beneath the Maturin Basin, north of the Orinoco River at 9°N and 62.75°W is a second, isolated high velocity body that extends from ~110 to >200 km depth (Fig. 5g, h, Fig. S3). We speculate that it is a Rayleigh–Taylor instability developing at the base of the

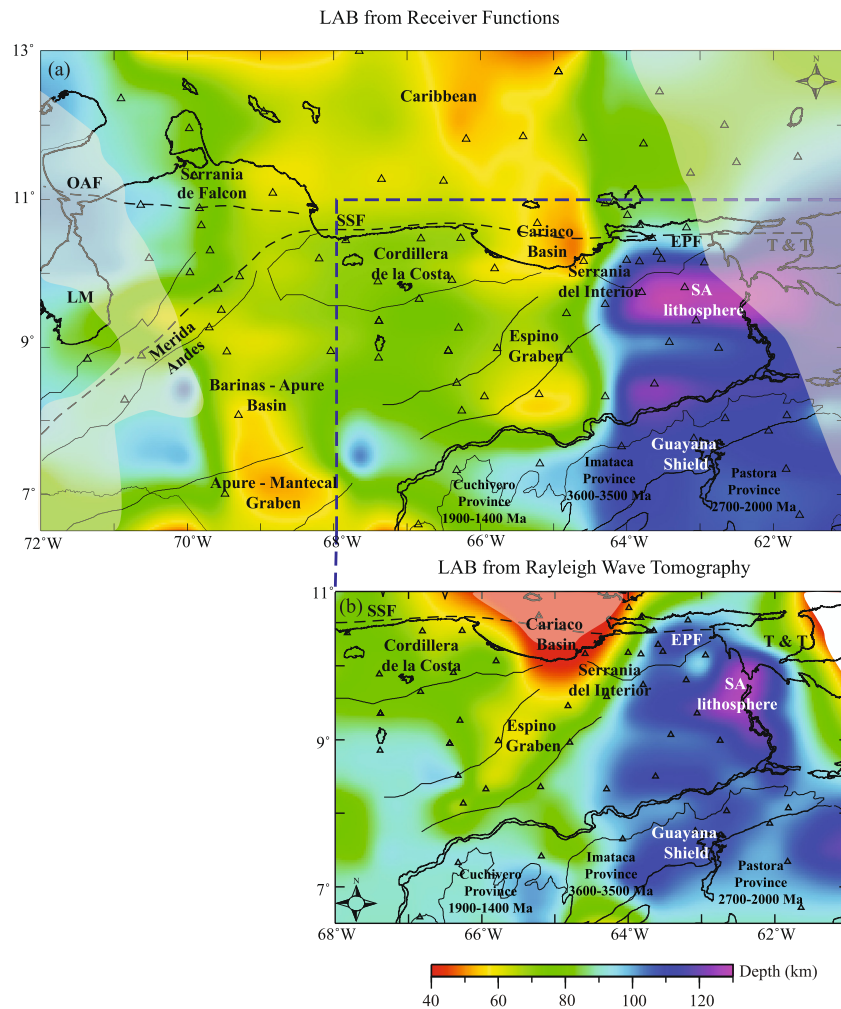


**Fig. 10.** Depth variations of the LAB estimated from receiver function images (a) and surface wave tomography (b). SA: South America; OAF: Oca-Ancon Fault; EPF: El Pilar Fault; SSF: San Sebastian Fault; T&T: Trinidad and Tobago. Blue box in (a) indicates the Rayleigh wave tomography study region. Translucent white mask shows areas where LAB is unconstrained. (For interpretation of the references to color in this figure legend, the reader is referred to the web version of this article.)

continental mantle lithosphere due to loading by the sediments in the Maturin basin, and possibly triggered by destabilization of the SA lithosphere induced by the descending Atlantic slab.

In addition to the two high-velocity anomalies, there is a pronounced low velocity zone (LVZ,  $\sim 4.3$  km/s) that extends to  $\sim 60$  km depth (Figs. 5 and 7) beneath the Cariaco basin. Miller et al. (2009) associated this LVZ with asthenospheric flow around the southern edge of the Atlantic plate resulting from slab roll-back. The Cariaco basin is known to be a transtensional basin resulting from a small right-step in the El Pilar fault. The low velocity anomaly could be associated with passive asthenospheric upwelling.

#### 4. Conclusions

We used Ps and Sp receiver functions and Rayleigh wave tomography to investigate the crust and upper-mantle velocity structure beneath Venezuela and southern Caribbean. The new seismic images allow us to reach five conclusions: (1) Lithospheric thickness is strongly correlated to geologic/tectonic province in northern South America. (2) In northwestern Venezuela the Ps receiver function images reveal a southeastward dipping interface, which can be interpreted as the Moho of the Caribbean plate under the northwestern Maracaibo block. (3) Lithospheric geometry and thickness is consistent with a slab tear under the Maracaibo block approximately beneath the Oca-Ancon fault. (4) In eastern

Venezuela, the surface wave tomography shows that the distinct high velocity anomaly associated with Atlantic subduction extends across the El Pilar fault, suggesting the base of SA continental margin mantle lithosphere descends with the Atlantic slab. (5) A subcontinental drip extending from the base of the lithosphere at  $\sim 110$  km to  $>200$  km may have developed beneath the Maturin basin, possibly due to a combination of loading of the basin and destabilization of the lithosphere by Atlantic subduction.

#### Acknowledgements

This project was supported by the NSF Continental Dynamics Program grants EAR-0607801 and EAR-0003572. FUNVISIS provided data from the Venezuela National Seismograph Network, and assistance during the field campaign. Gary Pavlis, Tammy Bravo, and Frank Vernon operated the PASSCAL and OBSIP instruments. Thanks to Maximiliano Bezada for providing the finite-frequency body wave tomography model, and to Maximiliano Bezada and Mariano Arnaiz for their comments and suggestions.

#### Appendix A. Supplementary material

Supplementary material related to this article can be found online at <http://dx.doi.org/10.1016/j.epsl.2014.08.041>.

## References

- Ammon, C., 1991. The isolation of receiver effects from teleseismic P waveforms. *Geol. Soc. Am. Bull.* 81 (6), 2504–2510.
- Audemard, F.E., Audemard, F.A., 2002. Structure of the Merida Andes, Venezuela: relations with the South Structure of the Me America–Caribbean geodynamic interaction. *Tectonophysics* 345, 299–327.
- Audemard, F.A., Romero, G., Rendon, H., Cano, V., 2005. Quaternary fault kinematics and stress tensors along the southern Caribbean from fault-slip data and focal mechanism solutions. *Earth-Sci. Rev.* 69 (3–4), 181–233. <http://dx.doi.org/10.1016/j.earscirev.2004.08.001>.
- Bezada, M.J., Levander, A., Schmandt, B., 2010a. Subduction in the southern Caribbean: images from finite-frequency P wave tomography. *J. Geophys. Res.* 115 (B12), 1–19. <http://dx.doi.org/10.1029/2010JB007682>.
- Bezada, M.J., Magnani, M.B., Zelt, C.A., Schmitz, M., Levander, A., 2010b. The Caribbean–South American plate boundary at 65°W: results from wide-angle seismic data. *J. Geophys. Res.* 115 (B8). <http://dx.doi.org/10.1029/2009JB007070>.
- Bezada, M.J., Schmitz, M., Jácome, M.I., Rodríguez, J., Audemard, F., Izarra, C., 2008. Crustal structure in the Falcón Basin area, northwestern Venezuela, from seismic and gravimetric evidence. *J. Geodyn.* 45 (4–5), 191–200. <http://dx.doi.org/10.1016/j.jog.2007.11.002>.
- Bijwaard, H., Spakman, W., Engdahl, E., 1998. Closing the gap between regional and global travel time tomography. *J. Geophys. Res.* 103, 30055–30078.
- Bilham, R., Mencin, D., 2013. Potential for great thrust earthquakes in NE Colombia and NE Venezuela. In: *AGU Meeting of the Americas*. Abstract T21A-01.
- Brocher, T.M., 2005. Empirical relations between elastic wavespeeds and density in the Earth's crust. *Geol. Soc. Am. Bull.* 95 (6), 2081–2092. <http://dx.doi.org/10.1785/0120050077>.
- Burke, K., 1977. Aulacogens and continental breakup. *Annu. Rev. Earth Planet. Sci.* 5, 371–396.
- Clark, S.A., Levander, A., Magnani, M.B., Zelt, C.A., 2008a. Negligible convergence and lithospheric tearing along the Caribbean–South American plate boundary at 64°W. *Tectonics* 27 (6), TC6013. <http://dx.doi.org/10.1029/2008TC002328>.
- Clark, S.A., Sobiesiak, M., Zelt, C.A., Magnani, M.B., Miller, M.S., Bezada, M.J., Levander, A., 2008b. Identification and tectonic implications of a tear in the South American plate at the southern end of the Lesser Antilles. *Geochem. Geophys. Geosyst.* 9 (11), Q11004. <http://dx.doi.org/10.1029/2008GC002084>.
- Clark, S.A., Zelt, C.A., Magnani, M.B., Levander, A., 2008c. Characterizing the Caribbean–South American plate boundary at 64°W using wide-angle seismic data. *J. Geophys. Res.* 113 (B7), 1–16. <http://dx.doi.org/10.1029/2007JB005329>.
- De Toni, B., Kellogg, J., 1993. Seismic evidence for blind thrusting of the Northwestern flank of the Venezuelan Andes. *Tectonics* 12 (6), 1393–1409.
- Dueker, K., Sheehan, A., 1997. Mantle discontinuity structure from midpoint stacks of converted P to S waves across the Yellowstone hotspot track. *J. Geophys. Res.* 102 (B4), 8313–8327. <http://dx.doi.org/10.1029/96JB03857>.
- Efron, B., Tibshirani, R., 1986. Bootstrap methods for standard errors, confidence intervals, and other measures of statistical accuracy. *Stat. Sci.* 1, 54–75.
- Escalona, A., Mann, P., Jaimes, M., 2011. Miocene to recent Cariaco basin, offshore Venezuela: structure, tectonosequences, and basin-forming mechanisms. *Mar. Pet. Geol.* 28 (1), 177–199. <http://dx.doi.org/10.1016/j.marpetgeo.2009.04.001>.
- Fischer, K.M., Ford, H.A., Abt, D.L., Rychert, C.A., 2010. The lithosphere–asthenosphere boundary. *Annu. Rev. Earth Planet. Sci.* 38 (1), 551–575. <http://dx.doi.org/10.1146/annurev-earth-040809-152438>.
- Forsyth, D.W., Li, A., 2005. Array analysis of two-dimensional variations in surface phase velocity and azimuthal anisotropy in the presence of multipathing interference. In: *Seismic Earth: Array analysis of Broadband Seismograms*. AGU, Washington, DC, pp. 81–97.
- Gonzales de Juana, C., Iturralde, J.M., Picard, X., 1980. *Geología de Venezuela y De Sus Cuencas Petrolíferas*. Ediciones Foninves, Caracas.
- Govers, R., Wortel, M.J.R., 2005. Lithosphere tearing at STEP faults: response to edges of subduction zones. *Earth Planet. Sci. Lett.* 236 (1–2), 505–523. <http://dx.doi.org/10.1016/j.epsl.2005.03.022>.
- Guedez, M.C., 2007. Crustal Structure Across the Caribbean–South America Plate boundary at 70°W—results from seismic refraction and reflection data. M.S. thesis. Dep. of Earth Science, Rice University, Houston, Texas, USA.
- Jácome, M.I., Kusznir, N., Audemard, F., Flint, S., 2003. Formation of the Maturín Foreland Basin, eastern Venezuela: thrust sheet loading or subduction dynamic topography. *Tectonics* 22 (5), 1046. <http://dx.doi.org/10.1029/2002TC001381>.
- Kellogg, J., Bonini, W., 1982. Subduction of the Caribbean Plate and Basement uplift in the Overriding South American Plate. *Tectonics* 1 (3), 251–276.
- Kennett, B.L.N., Engdahl, E.R., Buland, R., 1995. Constraints on seismic velocities in the Earth from traveltimes. *Geophys. J. Int.* 122, 108–124.
- Lee, C.-T.A., Luffi, P., Chin, E.J., 2011. Building and destroying continental mantle. *Annu. Rev. Earth Planet. Sci.* 39 (1), 59–90. <http://dx.doi.org/10.1146/annurev-earth-040610-133505>.
- Levander, A., Schmandt, B., Miller, M.S., Liu, K., Karlstrom, K.E., Crow, R.S., Lee, C.-T.A., Humphreys, E.D., 2011. Continuing Colorado plateau uplift by delamination-style convective lithospheric downwelling. *Nature* 472 (7344), 461–465. <http://dx.doi.org/10.1038/nature10001>.
- Levander, A., Schmitz, M., Ave Lallemand, H.G., Zelt, C.A., Sawyer, D.S., Magnani, M.B., Mann, P., Christerson, C., Wright, J., Pavlis, G., Pindell, J., 2006. Evolution of the southern Caribbean Plate boundary. *Eos Trans., AGU* 87 (9).
- Levander, A., Miller, M.S., 2012. Evolutionary aspects of lithospheric discontinuity structure in the western U.S. *Geochem. Geophys. Geosyst.* 13, Q0AK07. <http://dx.doi.org/10.1029/2012GC004056>.
- Ligorria, P., Ammon, C.J., 1999. Iterative deconvolution and receiver-function estimation. *Geol. Soc. Am. Bull.* 89 (5), 1395–1400.
- Liu, K., Levander, A., Niu, F., Miller, M.S., 2011. Imaging crustal and upper mantle structure beneath the Colorado Plateau using finite frequency Rayleigh wave tomography. *Geochem. Geophys. Geosyst.* 12 (7), Q07001. <http://dx.doi.org/10.1029/2011GC003611>.
- Magnani, M.B., Zelt, C.A., Levander, A., Schmitz, M., 2009. Crustal structure of the South American–Caribbean plate boundary at 67°W from controlled source seismic data. *J. Geophys. Res.* 114 (B2), 1–23. <http://dx.doi.org/10.1029/2008JB005817>.
- Malave, G., Suarez, G., 1995. Intermediate-depth seismicity in northern Colombia and western Venezuela and its relationship to Caribbean plate subduction. *Tectonics* 14 (3), 617–628.
- Masy, J., Niu, F., Levander, A., Schmitz, M., 2011. Mantle flow beneath northwestern Venezuela: seismic evidence for a deep origin of the Mérida Andes. *Earth Planet. Sci. Lett.* 305 (3–4), 396–404. <http://dx.doi.org/10.1016/j.epsl.2011.03.024>.
- McMahon, C.E., 2001. Evaluation of the effects of oblique collision between the Caribbean and South American Plates using geochemistry from Igneous and metamorphic bodies of Northern Venezuela. PhD thesis. Dep. of Civil Engineering and Geological Sciences, University of Notre Dame, Notre Dame, IN, USA.
- Meighan, H.E., ten Brink, U., Pulliam, J., 2013. Slab tears and intermediate depth seismicity. *Geophys. Res. Lett.* 40, 4244–4248. <http://dx.doi.org/10.1002/grl.50830>.
- Meschede, M., Frisch, W., 1998. A plate-tectonic model for the Mesozoic and Early Cenozoic history of the Caribbean plate. *Tectonophysics* 296, 269–291.
- Miller, M.S., Levander, A., Niu, F., Li, A., 2009. Upper mantle structure beneath the Caribbean–South American plate boundary from surface wave tomography. *J. Geophys. Res.* 114 (B1), B01312. <http://dx.doi.org/10.1029/2007JB005507>.
- Molnar, P., Sykes, L.R., 1969. Tectonics of the Caribbean and Middle America regions from focal mechanisms and seismicity. *Geol. Soc. Am. Bull.* 80 (9), 1639. [http://dx.doi.org/10.1130/0016-7606\(1969\)80<1639:TOTCAM>2.0.CO;2](http://dx.doi.org/10.1130/0016-7606(1969)80<1639:TOTCAM>2.0.CO;2).
- Niu, F., Bravo, T., Pavlis, G., Vernon, F., Rendon, H., Bezada, M., Levander, A., 2007. Receiver function study of the crustal structure of the southeastern Caribbean plate boundary and Venezuela. *J. Geophys. Res.* 112 (B11308), 1–15. <http://dx.doi.org/10.1029/2006JB004802>.
- Palma, M., Romero, G., 2011. Boletín Sismológico de Venezuela, Venezuelan. Found. for Seimolol. Res. (FUNVISIS). Available at: <http://www.funvisis.gob.ve/boletines.php>.
- Pennington, W., 1981. Subduction of the Eastern Panama Basin and seismotectonics of Northwestern South America. *J. Geophys. Res.* 86 (B11), 10753–10770.
- Perez, O., Bilham, R., Rebecca, B., Velandia, J.R., Napoleon, H., Mocayo, C., Hoyer, M., Kozuch, M., 2001. Velocity field across the southern Caribbean plate boundary and estimates of Caribbean/South-American plate motion using GPS geodesy 1994–2000. *Geophys. Res. Lett.* 28 (15), 2987–2990.
- Pindell, J., Kennan, L., Maresch, W.V., Stanek, K.-P., Draper, G., Higgs, R., 2005. Plate-kinematics and crustal dynamics of circum-Caribbean arc-continent interactions: tectonic controls on basin development in Proto-Caribbean margins. In: *Avé Lallemand, H.G., Sisson, V.B. (Eds.), Caribbean–South American Plate Interactions, Venezuela*. In: *Spec. Pap., Geol. Soc. Am.*, vol. 394, pp. 7–52.
- Russo, R.M., Speed, R.C., Okal, E.A., Shepherd, J.B., Rowley, K.C., 1993. Seismicity and tectonics of the southeastern Caribbean. *J. Geophys. Res.* 98 (B8), 14299. <http://dx.doi.org/10.1029/93JB00507>.
- Saito, M., 1988. DISPER80: a subroutine package for the calculation of seismic normal mode solutions. In: *Seismological Algorithms, Computational Methods and Computer Programs*. Academic, New York, pp. 293–319.
- Santamaria, F., Schubert, C., 1974. Geochemistry and geochronology of the southern Caribbean–northern Venezuela plate boundary. *Geol. Soc. Am. Bull.* 85 (7), 1085–1098. [http://dx.doi.org/10.1130/0016-7606\(1974\)85<1085>](http://dx.doi.org/10.1130/0016-7606(1974)85<1085>).
- Schmitz, M., Chalbaud, D., Castillo, J., Izarra, C., 2002. The crustal structure of the Guayana Shield, Venezuela, from seismic refraction and gravity data. *Tectonophysics* 345 (1–4), 103–118. [http://dx.doi.org/10.1016/S0040-1951\(01\)00208-6](http://dx.doi.org/10.1016/S0040-1951(01)00208-6).
- Schmitz, M., Martins, A., Izarra, C., Jácome, M.I., Sánchez, J., Rocabado, V., 2005. The major features of the crustal structure in north-eastern Venezuela from deep wide-angle seismic observations and gravity modelling. *Tectonophysics* 399 (1–4), 109–124. <http://dx.doi.org/10.1016/j.tecto.2004.12.018>.
- Schutt, D.L., Dueker, K., Yuan, H., 2008. Crust and upper mantle velocity structure of the Yellowstone hot spot and surrounding crusts. *J. Geophys. Res.* 113 (B3), B03310. <http://dx.doi.org/10.1029/2007JB005109>.
- Taboada, A., Rivera, L., Fuenzalida, A., Cisternas, A., Philip, H., Bijwaard, H., Olaya, J., Rivera, C., 2000. Geodynamics of the northern Andes: subductions and intracontinental deformation (Colombia). *Tectonics* 19 (5), 787–813. <http://dx.doi.org/10.1029/2000TC900004>.
- Urbani, F., 1989. Geothermal reconnaissance of northeastern Venezuela. *Geothermics* 18 (3), 403–427.

- Van Benthem, S., Govers, R., Spakman, W., Wortel, R., 2013. Tectonic evolution and mantle structure of the Caribbean. *J. Geophys. Res., Solid Earth* 118, 3019–3036.
- VanDecar, J.C., Russo, R.M., James, D.E., Ambeh, W.B., Franke, M., 2003. Aseismic continuation of the Lesser Antilles slab beneath continental South America. *J. Geophys. Res.* 108 (B1), 2043. <http://dx.doi.org/10.1029/2001JB000884>.
- Van Der Hilst, R.D., Mann, P., 1994. Tectonic implications of tomographic images of subducted lithosphere beneath northwestern South America. *Geology* 22, 451–454.
- Weber, J., Dixon, T., DeMets, C., Amberth, W., Jansma, P., Mattioli, G., Saleh, J., Sella, G., Bilham, R., Perez, O., 2001. GPS estimate of relative motion between the Caribbean and South American plates, and geologic implications for Trinidad and Venezuela. *Geology* 29, 75–78. [http://dx.doi.org/10.1130/0091-7613\(2001\)029<0075](http://dx.doi.org/10.1130/0091-7613(2001)029<0075).
- Yang, Y., Forsyth, D.W., 2006a. Rayleigh wave phase velocities, small-scale convection, and azimuthal anisotropy beneath southern California. *J. Geophys. Res.* 111 (B7), 1–20. <http://dx.doi.org/10.1029/2005JB004180>.
- Yang, Y., Forsyth, D.W., 2006b. Regional tomographic inversion of the amplitude and phase of Rayleigh waves with 2-D sensitivity kernels. *Geophys. J. Int.* 166 (3), 1148–1160. <http://dx.doi.org/10.1111/j.1365-246X.2006.02972.x>.
- Yoris, F., Ostos, M., 1997. Geología de Venezuela: geología general y cuencas petrolíferas. In: Singer, J. (Ed.), WEC 1997. Conferencia Evaluación de Pozos. Schlumberger – Sureco C.A. 1ra. Jolley Printing, Texas, pp. 24–44. Cap. 1: 1–17; Ed. Español.
- Yuan, H., Romanowicz, B., 2010. Lithospheric layering in the North American craton. *Nature* 466 (7310), 1063–1068. <http://dx.doi.org/10.1038/nature09332>.
- Yuan, X., Kind, R., Li, X., Wang, R., 2006. The S receiver functions: synthetics and data example. *Geophys. J. Int.* 165 (2), 555–564. <http://dx.doi.org/10.1111/j.1365-246X.2006.02885.x>.